Monthly Notices of the ROYAL ASTRONOMICAL SOCIETY

MNRAS **433,** 2693–2705 (2013)
Advance Access publication 2013 June 27

doi:10.1093/mnras/sts700

Bayesian constraints on dark matter halo properties using gravitationally lensed supernovae

N. V. Karpenka,[1★] M. C. March,[2] F. Feroz[3] and M. P. Hobson[3]

[1]*Department of Physics, The Oskar Klein Centre for Cosmoparticle Physics, Stockholm University, AlbaNova, SE-106 91 Stockholm, Sweden*
[2]*Astronomy Centre, University of Sussex, Brighton BN1 9QH, UK*
[3]*Astrophysics Group, Cavendish Laboratory, JJ Thomson Avenue, Cambridge CB3 0HE, UK*

Accepted 2012 December 21. Received 2012 December 20; in original form 2012 July 16

ABSTRACT

A hierarchical Bayesian method is applied to the analysis of Type Ia supernovae (SNIa) observations to constrain the properties of the dark matter haloes of galaxies along the SNIa lines of sight via their gravitational lensing effect. The full joint posterior distribution of the dark matter halo parameters is explored using the nested sampling algorithm MultiNest, which also efficiently calculates the Bayesian evidence, thereby facilitating robust model comparison. We first demonstrate the capabilities of the method by applying it to realistic simulated SNIa data, based on the real 3-year data release from the Supernova Legacy Survey (SNLS3). Assuming typical values for the parameters in a truncated singular isothermal sphere (SIS) halo model, we find that a catalogue analogous to the existing SNLS3 data set is typically incapable of detecting the lensing signal, but a catalogue containing approximately three times as many SNIa can produce robust and accurate parameter constraints and lead to a clear preference for the SIS halo model over a model that assumes no lensing. In the analysis of the real SNLS3 data, contrary to previous studies, we obtain only a very marginal detection of a lensing signal and weak constraints on the halo parameters for the truncated SIS model, although these constraints are tighter than those typically obtained from equivalent simulated SNIa data sets. This difference is driven by a preferred value of $\eta \approx 1$ in the assumed scaling law $\sigma \propto L^{\eta}$ between velocity dispersion and luminosity, which is somewhat higher than the canonical values of $\eta = \frac{1}{4}$ and $\eta = \frac{1}{3}$ for early and late-type galaxies, respectively.

Key words: gravitational lensing: weak – methods: data analysis – methods: statistical – supernovae: general – galaxies: haloes.

1 INTRODUCTION

In using Type Ia supernovae (SNIa) as 'standardizable' candles to constrain cosmological parameters, one typically assumes that the Universe is homogeneous and isotropic, and therefore one ignores gravitational lensing effects due to cosmic structure along the line of sight to each SNIa. In conventional cosmological SNIa analyses, this effect is usually regarded as an additional source of uncertainty, which adds extra scatter to the brightness of SNIa that increases with redshift (Kantowski, Vaughan & Branch 1995; Frieman 1996; Wambsganss et al. 1997; Holz & Wald 1998; Bergström et al. 2000). Fortunately, owing to flux conservation, the effects of gravitational magnification and demagnification average out and are therefore expected to lead to negligible bias in cosmological parameter estimates (see e.g. Jönsson et al. 2008; Sarkar et al. 2008).

Nonetheless, the gravitational lensing of SNIa can itself be used to constrain cosmology (Metcalf 1999; Dodelson & Vallinotto 2006; Zentner & Bhattacharya 2009) and/or the properties of the lensing matter (Rauch 1991; Metcalf & Silk 1999). In the latter case, one performs a complementary analysis to cosmological parameter estimation by instead assuming a particular background cosmological model (i.e. fixing the cosmological parameters to some concordance values) and using the observed distance moduli to constrain the nature of the cosmic structure, such as the properties of dark matter haloes, along the lines of sight to the SNIa. In principle, one might even hope to perform a joint analysis to constrain the background cosmological parameters and the nature of the cosmic structure simultaneously, but such an approach is likely to suffer from strong degeneracies between parameters.

An early tentative detection of gravitational lensing of SNIa was made by (Jönsson et al. 2007) using a sample from the Great Observatories Origins Deep Survey (GOODS; Riess et al. 2004; Strolger et al. 2004; Riess et al. 2007). More recently, Kronborg

★ E-mail: nkarp@fysik.su.se

© 2013 The Authors
Published by Oxford University Press on behalf of the Royal Astronomical Society

Downloaded from http://mnras.oxfordjournals.org/ at Stanford University on June 23, 2015

et al. (2010) focused on the detection of a gravitational lensing signal by assuming the properties of the dark matter haloes, fixing all the parameter values in the halo model to 'reasonable' values, and reported a positive result at the 99 per cent confidence level. Moreover, (Jönsson et al. 2010a) used 24 high-redshift ($0.4 \lesssim z \lesssim 1.8$) SNIa from GOODS to constrain the properties of dark matter haloes of galaxies also contained within GOODS. This study was extended in (Jönsson et al. 2010b) by using 175 high-redshift ($0.1 \lesssim z \lesssim 1$) SNIa from the 3-year data release of the Supernova Legacy Survey (SNLS3; Astier et al. 2006) to constrain the haloes of galaxies in the deep Canada–France–Hawaii Telescope Legacy Survey (CFHTLS) fields. Although the SNIa in SNLS are typically not as distant as those from GOODS, they are far more numerous and selected in a more homogeneous way. (Jönsson et al. 2010b) report the detection of a gravitational lensing signal at the 92 per cent confidence level, and place weak constraints on the parameters in their halo model.

In this paper, we also use high-redshift SNIa from SNLS3 to constrain the properties of dark matter haloes of galaxies in the CFHTLS fields that intersect the SNIa lines of sight. Our statistical methodology differs greatly, however, from that used by Jönsson et al. (2010a,b) and other previous studies. As recently discussed by March et al. (2011), the usual χ^2-method used to constrain cosmological parameters and/or the nature of cosmic structure from light-curve fits to SNIa observations (see e.g. Astier et al. 2006; Kowalski et al. 2008; Conley et al. 2011) suffers from some shortcomings in terms of its statistical foundations and robustness, including not allowing for rigorous model checking and not providing a reliable framework for the evaluation of systematic uncertainties. Consequently, we instead analyse the Spectrally Adaptive Light-curve Template (SALT)-II light-curve fits of the SNIa observations using the statistically principled and rigorous Bayesian hierarchical method (BHM) of March et al. (2011) to obtain a robust effective likelihood function giving the probability of obtaining the observed SNIa data (i.e. the parameter values obtained in the SALT-II light-curve fits) as a function of the parameters of the dark matter halo model assumed for the galaxies along the lines of sight to the SNIa. Moreover, rather than exploring the parameter space of the dark matter halo model using simple gridding methods (see e.g. Jönsson et al. 2010a,b), we instead sample from the full joint posterior distribution of the dark matter halo parameters using a nested sampling algorithm (Skilling 2004; Feroz & Hobson 2008; Feroz, Hobson & Bridges 2009). This enables us to explore all the halo model parameters simultaneously and allows for straightforward marginalization over subsets of them. The algorithm also efficiently calculates the Bayesian evidence, thereby facilitating robust model comparison.

The outline of this paper is as follows. In Section we give a brief summary of Bayesian inference methods, followed in Section by a description of our Bayesian methodology for using gravitational lensing of SNIa to constrain the properties of dark matter haloes of the galaxies intersecting the lines of sight. In Section 4, we describe the SNLS3 supernovae and galaxies data used in our analysis. We test the performance of our Bayesian methodology in Section 5 by applying it to realistic simulated data based on the real SNLS3 data, before analysing the real data sets and presenting our results in Section 6. We give our conclusions in Section 7.

Throughout the paper, we assume a spatially flat concordance Λcold dark matter background cosmology, characterized by the parameters $\mathcal{C} \equiv \{\Omega_{\mathrm{m},0}, \Omega_{\Lambda,0}, H_0\} = \{0.27, 0.73, 0.7\}$. Finally, we note that this paper may be considered as complementary to our companion paper (March et al. 2012), in which we use the BHM to analyse the SNLS3 catalogue, together with additional SNIa, particularly at low redshift, to constrain the background cosmological model, assuming no gravitational lensing along the lines of sight to the SNIa.

2 BAYESIAN INFERENCE

Our analysis methodology is built upon the principles of Bayesian inference, which provide a consistent approach to the estimation of a set of parameters $\boldsymbol{\Theta}$ in a model (or hypothesis) H for the data $\mathbf{D}$. Bayes' theorem states that

$$\Pr(\boldsymbol{\Theta}|\mathbf{D}, H) = \frac{\Pr(\mathbf{D}|\,\boldsymbol{\Theta}, H)\Pr(\boldsymbol{\Theta}|H)}{\Pr(\mathbf{D}|H)}, \tag{1}$$

where, for brevity, we denote $\Pr(\boldsymbol{\Theta}|\mathbf{D}, H) \equiv P(\boldsymbol{\Theta})$ as the posterior probability distribution of the parameters, $\Pr(\mathbf{D}|\boldsymbol{\Theta}, H) \equiv \mathcal{L}(\boldsymbol{\Theta})$ as the likelihood, $\Pr(\boldsymbol{\Theta}|H) \equiv \pi(\boldsymbol{\Theta})$ as the prior and $\Pr(\mathbf{D}|H) \equiv \mathcal{Z}$ as the Bayesian evidence.

In parameter estimation, the normalizing evidence factor is usually ignored, since it is independent of the parameters $\boldsymbol{\Theta}$, and inferences are often obtained by taking samples from the (unnormalized) posterior using standard MCMC sampling methods, where at equilibrium the chain contains a set of samples from the parameter space distributed according to the posterior. This posterior constitutes the complete Bayesian inference of the parameter values, and can be marginalized over each parameter to obtain individual parameter constraints.

In contrast to parameter estimation problems, for model selection the evidence takes the central role and is simply the factor required to normalize the posterior over $\boldsymbol{\Theta}$,

$$\mathcal{Z} = \int \mathcal{L}(\boldsymbol{\Theta})\pi(\boldsymbol{\Theta})\mathrm{d}^D\boldsymbol{\Theta}, \tag{2}$$

where D is the dimensionality of the parameter space. As the average of the likelihood over the prior, the evidence is larger for a model if more of its parameter space is likely and smaller for a model with large areas in its parameter space having low likelihood values, even if the likelihood function is very highly peaked. Thus, the evidence automatically implements Occam's razor. The question of model selection between two models H_0 and H_1 can then be decided by comparing their respective posterior probabilities given the observed data set $\mathbf{D}$, as follows:

$$R = \frac{\Pr(H_1|\mathbf{D})}{\Pr(H_0|\mathbf{D})} = \frac{\Pr(\mathbf{D}|H_1)\Pr(H_1)}{\Pr(\mathbf{D}|H_0)\Pr(H_0)} = \frac{\mathcal{Z}_1}{\mathcal{Z}_0}\frac{\Pr(H_1)}{\Pr(H_0)}, \tag{3}$$

where $\Pr(H_1)/\Pr(H_0)$ is the a priori probability ratio for the two models, which can often be set to unity but occasionally requires further consideration.

Evaluation of the multidimensional integral in equation (2) is a challenging numerical task. Standard techniques like thermodynamic integration are extremely computationally intensive which makes evidence evaluation at least an order of magnitude more costly than parameter estimation. Some fast approximate methods have been used for evidence evaluation, such as treating the posterior as a multivariate Gaussian centred at its peak (see e.g. Hobson & McLachlan 2003), but this approximation is clearly a poor one for multimodal posteriors (except perhaps if one performs a separate Gaussian approximation at each mode). The Savage–Dickey density ratio has also been proposed (see e.g. Trotta 2007) as an exact, and potentially faster, means of evaluating evidence, but is restricted to the special case of nested hypotheses and a separable prior on the model parameters. Various alternative information criteria for astrophysical model selection are discussed by Liddle (2007), but the evidence remains the preferred method.

Downloaded from http://mnras.oxfordjournals.org/ at Stanford University on June 23, 2015

The nested sampling approach, introduced by Skilling (2004), is a Monte Carlo method targeted at the efficient calculation of the evidence, but also produces posterior inferences as a by-product. Feroz & Hobson (2008) and Feroz et al. (2009) built on this nested sampling framework and have introduced the MultiNest algorithm which is very efficient in sampling from posteriors that may contain multiple modes and/or large (curving) degeneracies and also calculate the evidence. This technique greatly reduces the computational cost of Bayesian parameter estimation and model selection and has already been applied to a number of problems in astrophysics (see e.g. Bridges et al. 2009; Feroz et al. 2010; Feroz & Hobson 2012; Feroz, Balan & Hobson 2011). We employ this technique in this paper.

3 ANALYSIS METHODOLOGY

3.1 Definition of the SNIa data

In practice, there are no perfect astronomical standard candles. In particular, SNIa have absolute magnitudes that vary by about ± 0.8 mag in the B band due to physical differences in how each supernova is triggered and also due to absorption by its host galaxy. Nonetheless, SNIa do constitute a set of 'standardizable' candles, since by applying small corrections to their absolute magnitudes, derived by fitting multi-wavelengths observations of their light curves, one can reduce the scatter considerably, to around ± 0.15 mag in the B band. In essence, SNIa with broader light curves and slower decline rates are intrinsically brighter than those with narrower light curves and fast decline rates (Phillips 1993).

Several methods are available for fitting SNIa light curves (and constraining cosmological parameters), including, amongst others, the Multi-Colour Light curve Shape (MCLS) strategy (Jha, Riess & Kirshner 2007), Color-Magnitude Intercept Calibration (CMAGIC; Wang et al. 2003; Conley et al. 2006), and the SALT method (Guy et al. 2007), the current version of which is SALT-II. The relative merits of these methods is a topic of much debate, but the SALT-II method is particularly attractive for our purposes, since (unlike MCLS) it first fits each SNIa light curve to obtain three parameters controlling the SN magnitude, stretch and colour corrections to a template 'learned' from nearby and distant SN; only in a second, separate step are these fits used to constrain cosmological parameters. Following March et al. (2011), we may therefore use the products of the first step as the inputs to a statistically rigorous Bayesian hierarchical model.

Our analysis takes place after the selection cuts, light-curve fitting and Malmquist correction have been performed. For each selected SNIa, in addition to an estimate $\hat{z}$ of its redshift and an associated uncertainty σ_z, derived from observations of its host galaxy, we take as our basic data the output from the SALT-II light-curve fitting algorithm, which produces the best-fitting values: $\hat{m}^*_B$, the rest-frame B-band apparent magnitude of the supernovae at maximum luminosity; $\hat{x}_1$, the stretch parameter related to the width of the fitted light curve; and $\hat{c}$, the colour excess in the B band at maximum luminosity. These are supplemented by the covariance matrix of the uncertainties in the estimated light-curve parameters, namely

$$\widehat{C} = \begin{pmatrix} \sigma^2_{m^*_B} & \sigma_{m^*_B,x_1} & \sigma_{m^*_B,c} \\ \sigma_{m^*_B,x_1} & \sigma^2_{x_1} & \sigma_{x_1,c} \\ \sigma_{m^*_B,c} & \sigma_{x_1,c} & \sigma^2_{\mathrm{c}} \end{pmatrix}. \tag{4}$$

Therefore, our basic input data for each SN ($i = 1, \ldots, N_{\mathrm{SN}}$) are

$$D_i \equiv \{\hat{z}_i, \hat{m}^*_{B,i}, \hat{x}_{1,i}, \hat{c}_i\}, \tag{5}$$

and we assume (as is implicitly the case throughout the SNe literature) that the vector of values $(\hat{m}^*_{B,i}, \hat{x}_{1,i}, \hat{c}_i)$ for each SN is distributed as a multivariate Gaussian about the true values, with covariance matrix $\widehat{C}_i$. The 'observed' distance modulus μ_i^{obs} for each SN is then modelled as

$$\mu_i^{\mathrm{obs}} = \hat{m}^*_{B,i} - M_i + \alpha \hat{x}_{1,i} - \beta \hat{c}_i, \tag{6}$$

where M_i is the (unknown) B-band absolute magnitude of the SN, and α, β are (unknown) nuisance parameters (assumed the same for all SN) controlling the stretch and colour corrections.

It should be noted that a sophisticated BHM has recently been proposed by Mandel et al. (2009, 2010) to fit optical and infrared light-curve data. This may provide a more robust technique for defining the basic SNIa data that we use in our subsequent analysis, but we leave the investigation of this issue to a future work.

3.2 Computing the predicted distance moduli

In using SNIa to constrain cosmic structure, the predicted distance modulus must include the effect of gravitational magnification due to cosmic structure along the line of sight to each supernova. In particular, we assume this magnification is due to dark matter haloes associated with known galaxies intersecting the line of sight. Thus, for each SNIa, the predicted magnification depends on the sets of parameters $\{\boldsymbol{g}, \boldsymbol{h}\}$, where

$$\boldsymbol{g} = \left\{ z^1_{\mathrm{gal}}, \boldsymbol{\theta}^1_{\mathrm{gal}}, M^1_B, \tau^1, \ldots, z^{N_{\mathrm{gal}}}_{\mathrm{gal}}, \boldsymbol{\theta}^{N_{\mathrm{gal}}}_{\mathrm{gal}}, M^{N_{\mathrm{gal}}}_B, \tau^{N_{\mathrm{gal}}} \right\} \tag{7}$$

contains the redshift, sky position, absolute B-band magnitude and spectral type of the N_{gal} galaxies that intersect the line of sight to the SNIa, and $\boldsymbol{h}$ contains the parameters of the assumed dark matter halo model for these galaxies (see Section 3.3). In general, the parameters $\boldsymbol{g}$ are (naturally) different for each SN and are assumed known; one wishes to place constraints on the unknown halo parameters $\boldsymbol{h}$, which (perhaps unrealistically) are assumed common to all the foreground galaxies.

To compute the predicted magnification of a SNIa, we use the weak-lensing approximation (see e.g. Schneider, Ehlers & Falco 1992), the validity of which was checked by Jönsson et al. (2010b) by comparing it with a ray-tracing algorithm. For the SNIa sample we consider here (see Section 4.1), which have relatively low redshifts, the weak-lensing approximation was found to be accurate to within $\sim$5 per cent. In this approximation, the predicted distance modulus of a SNIa, expressed in terms of magnitudes, is related to the convergence κ along its line of sight by

$$\mu(z, \mathcal{C}, \boldsymbol{g}, \boldsymbol{h}) \approx \mu_0(z, \mathcal{C}) - 2.17[\kappa_{\mathrm{los}}(\boldsymbol{g}, \boldsymbol{h}) - \kappa_{\mathrm{b}}(\boldsymbol{h})], \tag{8}$$

where $\mu_0(z, \mathcal{C})$ is the predicted distance modulus for our assumed cosmological parameters $\mathcal{C}$, neglecting gravitational lensing, $\kappa_{\mathrm{los}}(\boldsymbol{g}, \boldsymbol{h})$ is a sum over the contributions to the convergence from each galaxy along the line of sight, so that $\kappa_{\mathrm{los}} = \sum_{j=1}^{N_{\mathrm{gal}}} \kappa^j_{\mathrm{gal}}$, and $\kappa_{\mathrm{b}}(\boldsymbol{h})$ represents the compensating effect of the background density and acts as a normalization allowing the magnification relative to a homogeneous universe to be computed (Jönsson et al. 2010b). Flux conservation implies that $\langle \kappa \rangle = 0$ and to ensure this condition is satisfied we set $\kappa_{\mathrm{b}}(\boldsymbol{h}) = \langle \kappa_{\mathrm{los}}(\boldsymbol{g}, \boldsymbol{h}) \rangle$, where the latter is calculated using a large number of randomly selected lines of sight.

Downloaded from http://mnras.oxfordjournals.org/ at Stanford University on June 23, 2015

3.3 Halo model

Our primary goal is to constrain the parameters $\boldsymbol{h}$ that describe the properties of the dark matter haloes associated with the galaxies along the lines of sight to the SNIa. We assume that each galaxy contributes to the convergence by an amount

$$\kappa_{\rm gal}(\boldsymbol{\xi}) = \frac{\Sigma(\boldsymbol{\xi})}{\Sigma_{\rm c}}, \tag{9}$$

where the surface density, $\Sigma(\boldsymbol{\xi})$, is obtained by projecting the matter distribution on to a lens plane,

$$\Sigma(\boldsymbol{\xi}) = \int_{-\infty}^{\infty} \rho(\boldsymbol{\xi}, y)\,{\rm d}y, \tag{10}$$

where $\boldsymbol{\xi}$ is a vector in the plane and y is a coordinate along the line of sight; it is at this point that the density profile $\rho(\boldsymbol{r})$ of the dark matter halo enters the calculation. The denominator in (9) is the critical surface density,

$$\Sigma_{\rm c} = \frac{c^2}{4\pi G}\frac{D_{\rm s}}{D_{\rm l}D_{\rm ls}}, \tag{11}$$

which, in turn, depends on the angular diameter distances between the observer and the source, $D_{\rm s}$, the observer and the lens, $D_{\rm l}$, and the lens and the source, $D_{\rm ls}$. These distances are computed from the redshifts of the SN and galaxy, respectively, assuming our concordance background cosmology.

In order to compare our results directly with those of (Jönsson et al. 2010a,b), in this paper we assume that the density profile $\rho(\boldsymbol{r})$ of the dark matter halo is described by a truncated singular isothermal sphere (SIS), although we note that our approach could be straightforwardly extended to consider alternative halo models, such as the Navarro–Frenk–White (NFW) profile (Navarro, Frenk & White 1997). The radial density distribution of a SIS is given by

$$\rho(r) = \frac{\sigma^2}{2\pi G}\frac{1}{r^2}, \tag{12}$$

which depends on the single free parameter σ, the one-dimensional velocity dispersion of its constituent particles. Since the SIS profile has a divergent total mass, we truncate it at a radius $r = r_{\rm t}$, which is thus a second free parameter.

The surface density of a truncated SIS is easily calculated using (10) and found to be

$$\Sigma(\xi) = \begin{cases} \frac{\sigma^2}{\pi G \xi}\arctan\sqrt{r_{\rm t}^2/\xi^2 - 1} & \text{if } \xi \le r_{\rm t} \\ 0 & \text{if } \xi > r_{\rm t}, \end{cases} \tag{13}$$

which can, in turn, be substituted into (9) to obtain the convergence $\kappa_{\rm gal}(\xi)$ due to the galaxy dark matter halo.

To allow for and investigate the relationship between galaxy luminosity and velocity dispersion, we follow (Jönsson et al. 2010b) and adopt the Faber–Jackson (Faber & Jackson 1976) and Tully–Fisher-like (Tully & Fisher 1977) scaling law

$$\sigma = \sigma_* \left(\frac{L}{L_*}\right)^{\eta}, \tag{14}$$

where L_* is a fiducial luminosity, which we take to be $L_* = 10^{10}\,h^{-2}\,{\rm L}_\odot$ in the B band, and σ_* is the corresponding fiducial velocity dispersion. In terms of absolute B-band magnitudes, with which we will be working, the scaling relation becomes

$$\sigma = \sigma_* 10^{-\eta(M_B - M_B^*)/2.5}, \tag{15}$$

where $M_B^* = -19.52 + 5\log_{10} h$ and h is the Hubble constant in units of 100 km s^{-1} Mpc^{-1}. The (aperture) mass-to-light ratio of the galaxies is determined by η, since

$$\frac{M(r \le R)}{L} = \frac{2\sigma_*^2 (L/L_*)^{2\eta} R}{GL} \propto L^{2\eta - 1}, \tag{16}$$

provided $R \le r_{\rm t}$. Thus, for example, one has a constant mass-to-light ratio $M/L \propto L^0$ if $\eta = 0.5$.

For the truncation radius, we again follow Jönsson et al. (2010b) and assume it obeys a scaling law of the form[1]

$$r_{\rm t} = r_* \left(\frac{\sigma}{\sigma_*}\right)^{\gamma} = r_* \left(\frac{L}{L_*}\right)^{\eta\gamma}, \tag{17}$$

where r_* is a fiducial truncation radius. Since we only include galaxies located a distance $\theta_{\rm c}$ from the position of the SN Ia, the truncation radius has an effect only if $r_{\rm t}/D_{\rm d} < \theta_{\rm c}$. For $\theta_{\rm c} = 60$ arcsec and $z_{\rm gal} < 1$ this corresponds to $r_{\rm t} \lesssim 300\,h^{-1}$ kpc.

Thus, for the truncated SIS halo model, we wish to constrain the four parameters $\boldsymbol{h} = \{\gamma, \eta, \sigma_*, r_*\}$.

3.4 Likelihood function

To construct the likelihood function for the SNIa data, we adopt the Bayesian hierarchical model proposed by March et al. (2011). This has been shown to deliver tighter constraints on cosmological parameters than the usual χ^2-method, and simultaneously provides a robust statistical framework for the full propagation of systematic uncertainties to the final inferences.

We require the likelihood of the input data (5) for our full catalogue of SNe, given the parameters of our model, namely

$$\Pr(\hat{\boldsymbol{m}}_B^*, \hat{\boldsymbol{x}}_1, \hat{\boldsymbol{c}}, \hat{\boldsymbol{z}} | \boldsymbol{h}, \alpha, \beta, \sigma_{\rm int}), \tag{18}$$

which also depends on the cosmological parameters $\mathcal{C}$, the covariance matrices $\widehat{C}_i$ of the uncertainties on the input data $(\hat{m}_{B,i}^*, \hat{x}_{1,i}, \hat{c}_i)$ for each SN, and the uncertainties $\sigma_{z,i}$ in the estimated redshifts $\hat{z}_i$, all of which are assumed known. In particular, we seek to constrain the unknown halo parameters $\boldsymbol{h}$, global colour and stretch correction multipliers α and β, and the intrinsic dispersion $\sigma_{\rm int}$ of SNIa absolute magnitudes (all of these are assumed to be 'global' parameters, i.e. common to every SN).

Following March et al. (2011), we compute the likelihood (18) by first introducing for each SN the hidden variables M_i, x_i, c_i and z_i, which are, respectively, the true (unknown) values of its absolute B-band magnitude, stretch and colour corrections, and redshift. These are then assigned priors, which themselves contain further nuisance parameters, and all the introduced parameters are marginalized over to obtain the likelihood (18). The details of this procedure are given in Appendix B of our companion paper (March et al. 2012). By assuming separable Gaussian priors on the hidden variables and nuisance parameters, one can perform all the marginalizations analytically, except for two nuisance parameters R_x and $R_{\rm c}$ (the dispersions of the priors on the stretch and colour corrections, respectively) that must be marginalized over numerically. The full likelihood function thus depends on the parameters $\boldsymbol{\Theta} = \{\boldsymbol{h}, \alpha, \beta, \sigma_{\rm int}, R_x, R_{\rm c}\}$, and is nine-dimensional for the truncated SIS halo model.

[1] One could assume a $r_{\rm t}$–L relationship, to break the coupling between η and γ, but this would make comparison with Jönsson et al. (2010b) difficult.

Downloaded from http://mnras.oxfordjournals.org/ at Stanford University on June 23, 2015

Table 1. Priors on the nuisance parameters and the halo parameters of the truncated SIS model, where $\mathcal{U}(a, b)$ denotes a uniform distribution between the limits a and b.

Parameter	Symbol	Prior
Nuisance parameters		
Dispersion of absolute magnitude	$\sigma_{\rm int}$	$\mathcal{U}(-3, 0)$ on $\ln \sigma_{\rm int}$
Stretch multiplier	α	$\mathcal{U}(0, 4)$
Colour multiplier	β	$\mathcal{U}(0, 4)$
Dispersion of stretch correction	R_x	$\mathcal{U}(-5, 2)$ on $\ln R_x$
Dispersion of colour correction	$R_{\rm c}$	$\mathcal{U}(-5, 2)$ on $\ln R_{\rm c}$
Halo parameters		
Fiducial velocity dispersion (km s^{-1})	σ_*	$\mathcal{U}(0, 300)$
Fiducial truncation radius (Mpc)	r_*	$\mathcal{U}(0, 0.4)$
Exponent of $\sigma - L$ power law	η	$\mathcal{U}(-2, 2)$
Exponent of $r_{\rm t} - \sigma$ power law	γ	$\mathcal{U}(-5, 5)$

3.5 Priors on the sampled parameters

To determine the Bayesian inference problem completely, it only remains to specify the prior $\pi(\boldsymbol{\Theta})$ on the parameters to be sampled. The choice of prior is particularly important for weak lensing analyses, since the problem is inherently underconstrained and therefore any prior information available is extremely useful. One should, however, be careful in the choice of priors not to impose too strong assumptions, which may lead to erroneous inferences.

Following March et al. (2011), we adopt the separable priors listed in Table 1 on each of the 'non-halo' (nuisance) parameters $\sigma_{\rm int}$, α, β, R_x and $R_{\rm c}$, and on the halo parameters $\boldsymbol{h}$ for the truncated SIS model; these correspond to broad, conservative assumptions.

4 SUPERNOVAE AND GALAXIES DATA SETS

To apply the Bayesian analysis methodology described above to constrain the dark matter haloes of galaxies, we need observations of both supernovae and foreground galaxies. As in Jönsson et al. (2010b), we use high-redshift ($0.1 \lesssim z \lesssim 1$) SNIa from the 3-year SNLS data set (Guy et al., in preparation) to constrain the properties of dark matter haloes of galaxies in the CFHTLS fields that intersect the SNIa lines of sight.

The SNLS consists of both photometric and spectroscopic observations. The photometry is obtained as part of the deep component of CFHTLS with the 1 deg^2 imager MegaCam (Boulade et al. 2003). The deep part of CFHTLS comprises four fields (D1, D2, D3 and D4), each ≈ 1 deg^2 in size, imaged in u^*, g', r', i' and z' filters approximately every 4–5 d during dark and grey time, suitable for detecting supernovae and building light curves (Astier et al. 2006; Guy et al., in preparation). The spectroscopic observations are used to determine the nature of the supernovae candidates and measure their redshifts (Howell et al. 2005; Bronder et al. 2008; Balland et al. 2009).

4.1 Supernovae

Our initial sample consisted of 230 high-redshift ($0.1 \lesssim z \lesssim 1$) SNIa from the 3-year SNLS data set (Guy et al., in preparation). We note that this is 13 fewer than available to Jönsson et al. (2010b), since these SNIa were excluded from the SALT-II fits for various reasons described in Conley et al. (2011), and do not appear in the tables in that paper. The sample of 230 SNIa is further reduced, however, by edge effects and by some parts of the deep CFHTLS fields being covered by bright stars that have to be masked (Sullivan et al. 2006). SNIa located too close to the boundary of the field or to a masked region are removed from the sample because of the lack of observations of foreground galaxies. Details of this procedure are given in Jönsson et al. (2010b). Only 162 of the initial sample of 230 SNIa fulfilled this selection criterion.

To compute the predicted magnification due to the foreground galaxies along the line of sight to each SNIa, we require an estimate of its sky location $\boldsymbol{\theta}_{\rm SN}$ and redshift $\hat{z}_{\rm SN}$. The sky location is obtained from the CFHTLS i'-band photometry. When available, $\hat{z}$ is taken to be the spectroscopic redshift of the SNIa host galaxy; otherwise the spectroscopic redshift of the SNIa itself is used.

Selection cuts, SALT-II light-curve fitting and Malmquist corrections are made by the SNLS3 team and are already implemented in the supplied data files. As described in Section 3.1, the SALT-II fitting algorithm is applied to each SNIa light curve to obtain best-fitting estimates of: $\hat{m}_B^*$, the rest-frame B-band apparent magnitude of the supernovae at maximum luminosity; $\hat{x}_1$, the stretch parameter of the fitted light curve; and $\hat{c}$, the colour excess in the B band at maximum luminosity. These are supplemented by the covariance matrices $\widehat{C}$ of the uncertainties in the estimated light-curve parameters, which are taken from Conley et al. (2011).

4.2 Galaxies

Our foreground galaxies are taken from the SNLS galaxy catalogues in the deep CFHTLS fields. As discussed in Section 3.2, to perform our analysis we require for each galaxy: the redshift $z_{\rm gal}$, sky position $\boldsymbol{\theta}_{\rm gal}$, absolute B-band magnitude M_B, and spectral type τ. The techniques used to obtain these galaxy properties are described in detail in Sullivan et al. (2006) and Jönsson et al. (2010b).

5 APPLICATION TO SIMULATED SUPERNOVAE DATA

In order to test our Bayesian analysis methodology, we first apply it to simulated SNIa data. First, SNIa photometric data in the absence of gravitational lensing were simulated and fitted using the publicly available SNANA package (Kessler et al. 2009), in an identical manner to that described in our companion paper (March et al. 2012). In summary, the data were simulated to match closely the SNLS3 data set (Guy et al. 2010) by using the SNLS3 co-added simulation library files (which are publicly available as part of the SNANA package), a coherent magnitude smearing of 0.12, and colour smearing. The colour smearing effect, or broad-band colour dispersion model, implemented in the data simulation is the exponential of a polynomial (EXPPOL) model described by fig. 8 of (Guy et al. 2010), and the simulated Malmquist bias is based on fig. 14 of Perrett et al. (2010).

The SNANA SNIa data simulation is a two-stage process that mimics the real data collection and analysis process. The first stage is the simulation of photometric data in accordance with the characteristic instrument and survey properties of the SNLS3 survey using the SNLS3 simulation library files mentioned above. The second stage is the light-curve fitting process in which the photometric data are fitted to SALT-II templates to give estimates of the SNIa absolute B-band magnitude $\hat{m}_B$, light-curve stretch $\hat{x}_1$ and colour $\hat{c}$. At this light-curve fitting stage, basic cuts are made to discard SNIa with a low signal-to-noise ratio and/or too few observed epochs in sufficient bands. After the light-curve fitting stage we make a redshift-dependent magnitude correction to correct for the Malmquist bias; the correction is taken from a spline interpolation of table 4 in Perrett et al. (2010).

Downloaded from http://mnras.oxfordjournals.org/ at Stanford University on June 23, 2015

Table 2. Halo parameter values used in the generation of simulated gravitationally lensed SNIa data.

Halo parameter	Symbol	Value
Fiducial velocity dispersion (km s^{-1})	σ_*	120
Fiducial truncation radius (Mpc)	r_*	0.07
Exponent of $\sigma - L$ power law	η	$\frac{1}{3}$
Exponent of $r_t - \sigma$ power law	γ	1

The resulting simulated SNIa are randomly distributed on the sky across the four SNLS3 fields, outside of our masked regions, and have a redshift distribution appropriate for the SNLS3 survey; in total we simulate 10^4 SNIa. The final stage of our simulation process adds the lensing contribution due to the (assumed) galaxy haloes along the line of sight to each SN. This is performed using the *real* SNLS galaxy catalogue by assuming each galaxy to have a halo described by a truncated SIS profile with the parameter values listed in Table 2. The choice of the velocity dispersion σ_* and truncation radius r_* corresponds to the best-fitting values obtained by (Jönsson et al. 2010b). The value $\eta = \frac{1}{3}$ corresponds to the Tully–Fisher relation for late-type galaxies, which should make up the majority of the SNLS sample, since nearly 95 per cent of them are star-forming galaxies. We also assume $\gamma = 1$, which corresponds to the truncation radius being linearly proportional to σ, and has the natural consequence that the halo mass scales as $M \propto \sigma^3$. For an assumed set of halo parameters, the lensing contribution from the haloes along the line of sight to each simulated SN is then added to the SN apparent magnitude, and its uncertainty is left unchanged.

5.1 Characteristics of the lensing signal

Before we apply our BHM to sets of simulated supernovae data, it is of interest first to investigate the general characteristics of the simulated lensing signal. It is worth reiterating that this signal is calculated for each of the 10^4 simulated SNIa using the *true* galaxies from the SNLS catalogue along each line of sight, albeit with the assumption that each such galaxy has a dark matter halo described by a truncated SIS profile with the fiducial parameter values given in Table 2.

In Fig. 1 (top panel), we plot the magnification factor for each of the 10^4 simulated SNIa. We note, in particular, that most of the SNIa are demagnified, as a result of the background correction described in Section 3.2, but a small number of SNIa are significantly magnified. When analysing random samples of (say) a few hundred SNIa, one would therefore expect a wide variation in the significance at which one detects a gravitational lensing signal, depending on whether the sample contains one or more of the SNIa that are strongly magnified.

We note further that, for the significantly lensed SNIa, there is no clear correlation between the size of the magnification and redshift, suggesting that high-redshift SNIa are not necessarily to be preferred for detecting the lensing signal of dark matter haloes. It is of interest to investigate further the lines of sight along which there is a significant lensing effect. In Fig. 1 (bottom panel), we plot the magnification as a function of redshift along the 75 lines of sight that exhibit the highest magnification. Although the magnification of the three most highly lensed lines of sight continues to increase markedly up to $z = 1$, the magnification along the remaining lines of sight typically does not increase appreciably beyond $z \sim 0.5$, again showing that high-redshift SNIa are not necessarily of more use in detecting the lensing signal.

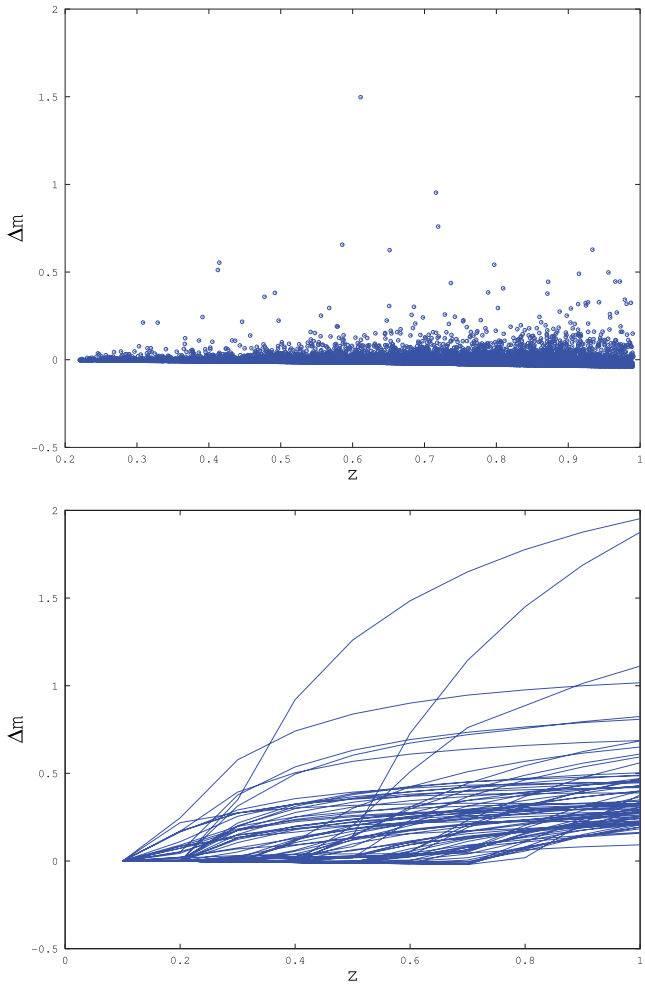

Figure 1. Top: magnification of 10^4 simulated SNIa randomly positioned in the true SNLS galaxy catalogue, and drawn from a redshift distribution appropriate for the SNLS3 supernovae survey. Bottom: magnification versus redshift for the 75 lines of sight that exhibit the strongest simulated lensing effect.

5.2 Results for random samples of 162 supernovae

In Fig. 2, we plot the histogram of the log-evidence difference $\Delta \ln \mathcal{Z}$, for the SIS halo model relative to the null (no-lensing) model, obtained from the analysis of 100 random samples of 162 SNIa (to match the number in the real SNLS3 sample to be analysed in Section 6). As anticipated, there is a large variation, with $\Delta \ln \mathcal{Z}$ ranging from about -1.5 to 4.5. According to Jeffreys' scale, the former corresponds to the SIS halo model being 'substantially' disfavoured, whereas as the latter indicates that it is 'very strongly' preferred, relative to the no-lensing model. We note that the histogram has a median -0.6, mean -0.3 and standard deviation 1.0. We also find that the random samples having large values of $\Delta \ln \mathcal{Z}$ typically contain a number of the most strongly lensed SNIa.

For the random sample that yields the median value of $\Delta \ln \mathcal{Z} = -0.6$, we plot the corresponding parameter constraints for the SIS halo model in Fig. 3, derived from the analysis of data with and without the lensing signal, respectively. One sees that the parameter constraints derived in each case are quite similar, suggesting that a SNLS-quality catalogue containing just 162 SNIa is unlikely to constrain the halo properties. Indeed this is what one might expect for a SNIa sample for which $\Delta \ln \mathcal{Z} = -0.6$, indicating that the

Downloaded from http://mnras.oxfordjournals.org/ at Stanford University on June 23, 2015

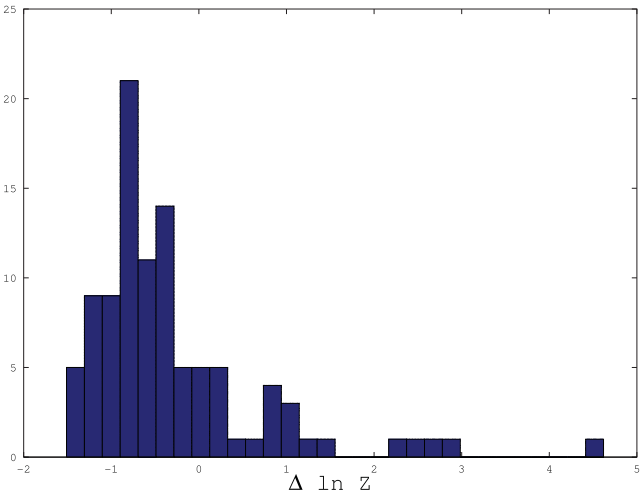

Figure 2. Histogram of the log-evidence difference $\Delta \ln \mathcal{Z}$ between the SIS halo model and the null (no-lensing) model obtained from the analysis of 100 random samples of 162 SNIa.

SIS halo model is marginally disfavoured relative to the no-lensing model.

In particular, we see that the 1D marginals for σ_* and r_* both peak at zero (which corresponds to no lensing signal), although the former does have a modest subsidiary peak at the correct input value of σ_* for the data containing the lensing signal. Another noteworthy feature is that, whereas the value of η is unconstrained, there is quite a strong constraint restricting γ to be negative. From (17), one sees that this corresponds to a rather curious truncation radius scaling law, for which galaxies with larger velocity dispersions have smaller truncation radii. Moreover, provided η is positive, this also corresponds to more luminous (and presumably more massive) galaxies having smaller truncation radii. This phenomenon was also noted by Jönsson et al. (2010b), but was erroneously interpreted as being a constraint on the halo properties derived from the SNIa data, which is clearly not the case, since it occurs even in the analysis of simulations containing no lensing signal. Rather, from (13) and (17), one sees that a negative value of γ allows for a smaller value of the truncation radius r_t to 'offset' an increase in the velocity dispersion σ, thereby reducing the lensing signal produced by the putative halo, as required to be consistent with simulated data containing no lensing signal.

In any Bayesian model selection analysis, it is instructive to investigate the impact of our assumed priors, listed in Table 1, on the value of $\Delta \ln \mathcal{Z}$. Since we are concerned only with the relative evidence between the SIS halo model and the model assuming no lensing, we need not consider the priors on the nuisance parameters, since these are common to both models. For the halo parameters, the range of the uniform priors on σ_* and r_* is reasonably uncontroversial and motivated by both physical considerations and previous studies. For the power-law exponents η and γ, however, our prior knowledge is far less certain and, as commented above, the constraints on these parameters shown in Fig. 3 display some unusual features. We therefore confine our attention to these parameters.

In Fig. 4, we plot $\Delta \ln \mathcal{Z}$ for the 'median' sample of 162 SNIa as a function of the (symmetric positive and negative) limits on the uniform priors assumed for η and γ. In particular, one sees that as the prior limits on γ are increased, $\Delta \ln \mathcal{Z}$ also increases, indicating an improvement in the quality of the fit to the data that outweighs the Occam's razor penalty of widening the prior range. This behaviour, although unusual, may be understood from the parameter constraints plotted in Fig. 3, which show a clear preference for large negative values of γ, as discussed above. Moreover, provided the prior on γ is wider than about $\pi(\gamma) = \mathcal{U}(-3, 3)$, there is little

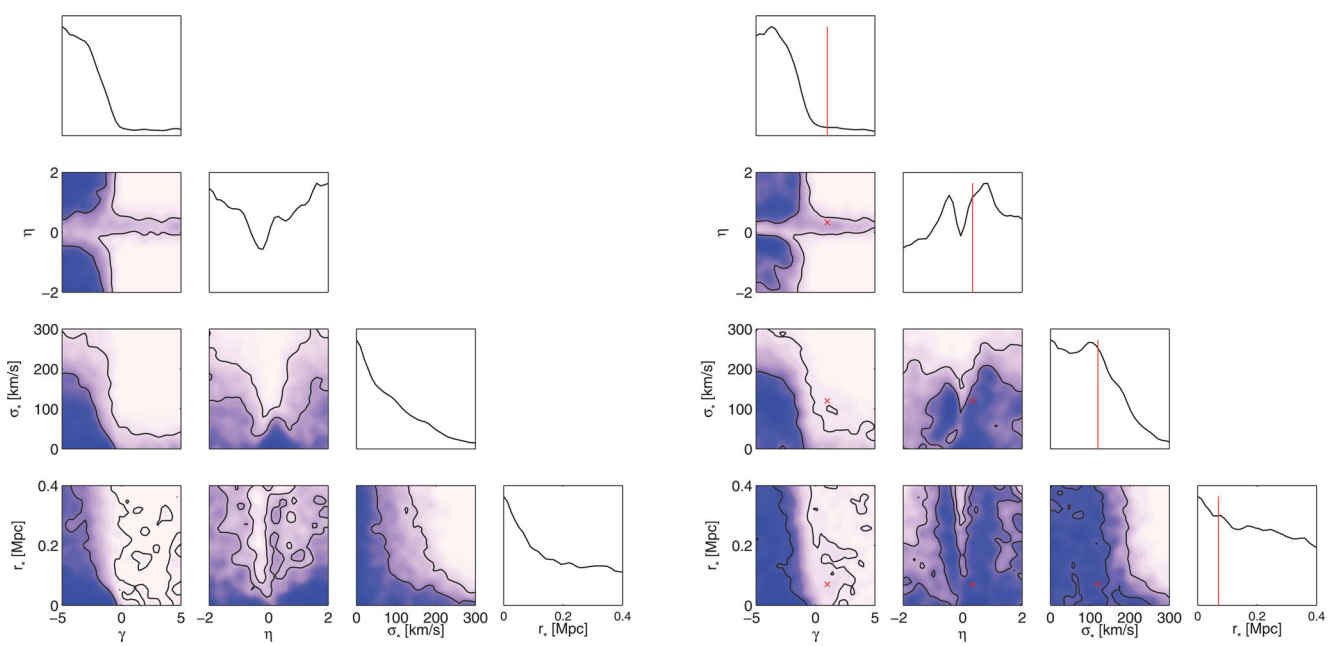

Figure 3. 1D and 2D marginalized posterior distributions for the parameters $\boldsymbol{h} = \{\gamma, \eta, \sigma_*, r_*\}$ of the truncated SIS halo model, derived from the analysis of 162 simulated SNIa data generated assuming no lensing (left) and a truncated SIS model (right). In the right-hand panel, true parameters are indicated by vertical lines and crosses in 1D and 2D plots, respectively. The SNIa sample used corresponds to that with the median value $\Delta \ln \mathcal{Z} = -0.6$ from the histogram in Fig. 2.

Downloaded from http://mnras.oxfordjournals.org/ at Stanford University on June 23, 2015

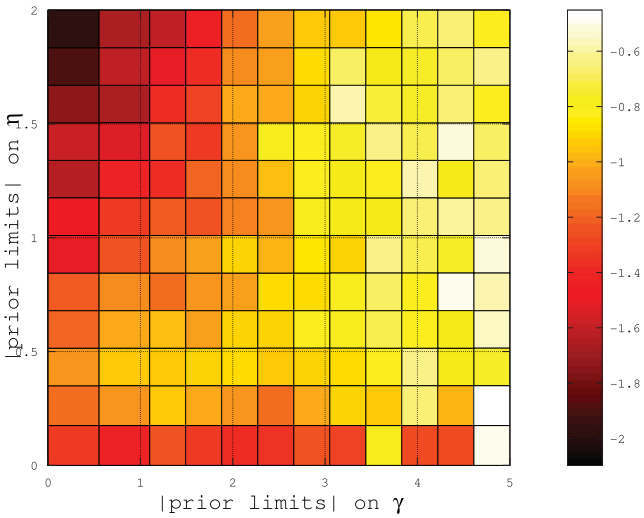

Figure 4. Log-evidence difference $\Delta \ln \mathcal{Z}$ between the SIS halo model and the null for the 'median' sample of 162 SNIa, as a function of the (symmetric positive and negative) limits on the uniform priors assumed for the parameters η and γ.

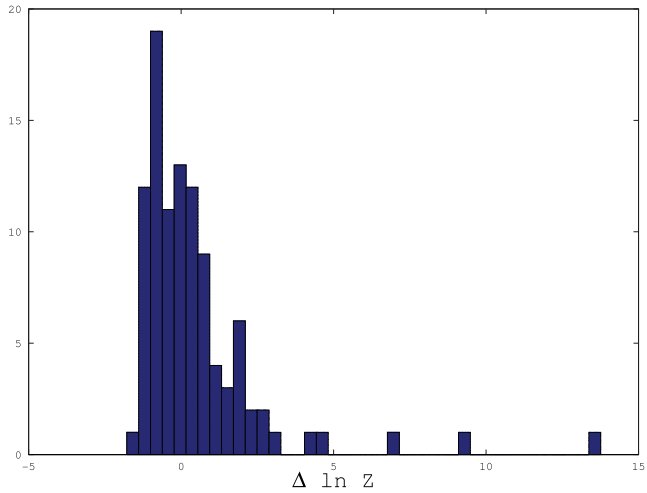

Figure 5. Histogram of the log-evidence difference $\Delta \ln \mathcal{Z}$ between the SIS halo model and the null (no-lensing) model obtained from the analysis of 100 random samples of 500 SNIa.

dependence of $\Delta \ln \mathcal{Z}$ on the width of the prior on η. For narrow priors on γ, however, one sees that there is a broad peak in $\Delta \ln \mathcal{Z}$ centred on priors for η of around $\pi(\eta) = \mathcal{U}(-\frac{1}{2}, \frac{1}{2})$, which is just sufficient to encompass the posterior probability mass associated with the true input value of $\eta = 1/3$. Narrower priors on η produce smaller values of $\Delta \ln \mathcal{Z}$ since they do not contain this probability mass, whereas wider priors on η lead to smaller values of $\Delta \ln \mathcal{Z}$ since they incur an Occam's razor penalty for increasing the extent of the prior without obtaining a compensating improvement in the quality of the fit to the data. Finally, we note that in all cases, $\Delta \ln \mathcal{Z}$ remains negative, showing that the SIS halo model is disfavoured relative to the no-lensing model.

5.3 Results for 162 SNLS3-like supernovae

To match the real SNLS3 data to be analysed in Section 6, we also constructed a simulation containing 162 SNIa, with positions on the sky and redshifts fixed to those of the real 162 SNLS3 SNIa. The parameter constraints obtained in the analysis of data, with and without a simulated lensing signal, are very similar to those obtained for the 'median' sample of 162 SNIa, shown in Fig. 3, so we do not plot them here.

In this case, the Bayesian log-evidence for the SIS halo model, relative to the null (no-lensing) model, is found to be $\Delta \ln \mathcal{Z} = -1.3 \pm 0.2$ for the data set containing a simulated lensing signal. Thus, according to the Jeffrey's scale, the no-lensing model is 'substantially' preferred (just) over the SIS halo model. This again suggests that the quantity and quality of the real SNLS3 data to be analysed in Section 6 are insufficient to obtain a detection of the lensing signal assumed in the simulation. Indeed, we note that the value of $\Delta \ln \mathcal{Z}$ obtained lies near the low end of the range of those for the 100 random samples of 162 SNIa, as plotted in Fig. 2. Nonetheless, when the limits on the uniform priors for η and γ are allowed to vary, one obtains a similar variation of $\Delta \ln \mathcal{Z}$ to that displayed in Fig. 4; we therefore do not plot it here.

5.4 Results for random samples of 500 supernovae

To test that our analysis procedure is capable of detecting the gravitational lensing signal and placing the correct constraints on halo parameters in the presence of more data, we also analyse simulated random samples of 500 SNIa, which contain approximately three times the number of SNIa as considered previously and is thus representative of what could be achieved by the SLNS programme in a total of about 9 years of observation. This is clearly rather unrealistic in terms of the required observing time and resources, but still provides a useful insight into the quantity of SNIa data required to make a robust detection of the lensing signal and constrain halo properties.

In Fig. 5, we plot the histogram of the log-evidence difference $\Delta \ln \mathcal{Z}$, for the SIS halo model relative to the null (no-lensing) model, obtained from the analysis of 100 random samples of 500 SNIa. Once again, the $\Delta \ln \mathcal{Z}$ values vary considerably between samples, ranging from about -2 to 13. The histogram has a median 0.1, mean 0.5 and standard deviation 2.1, showing that, as expected, the distribution is shifted to larger values of $\Delta \ln \mathcal{Z}$, as compared to the corresponding histogram in Fig. 2, obtained from random samples of 162 SNIa. Also, the high-end of the distribution contains a small number of samples for which $\Delta \ln \mathcal{Z}$ is very large, indicating a 'decisive' preference for the SIS halo model over the no-lensing model. Nonetheless, the lower end of the distribution extends as far as that obtained for random samples of 162 SNIa, and contains samples for which the SIS halo model is still 'substantially' disfavoured. We again find that the key factor in determining the value of $\Delta \ln \mathcal{Z}$ for a given sample is whether it contains some of the most strongly lensed SNIa. Hence, one's ability to detect and characterize the gravitational lensing signal from putative dark matter haloes is less a matter of how many SNIa one observes, but rather whether one's sample contains some highly magnified examples, although, clearly, the chances of finding such SNIa increases with the total number observed. Moreover, highly magnified SNIa do not appear to be concentrated at particularly high redshifts, so the importance of observing high-redshift SNIa is not clear in this application.

For the random sample that yields the median value of $\Delta \ln \mathcal{Z} = 0.1$, we plot the corresponding parameter constraints for the SIS halo model in Fig. 6, derived from the analysis of data with a

Downloaded from http://mnras.oxfordjournals.org/ at Stanford University on June 23, 2015

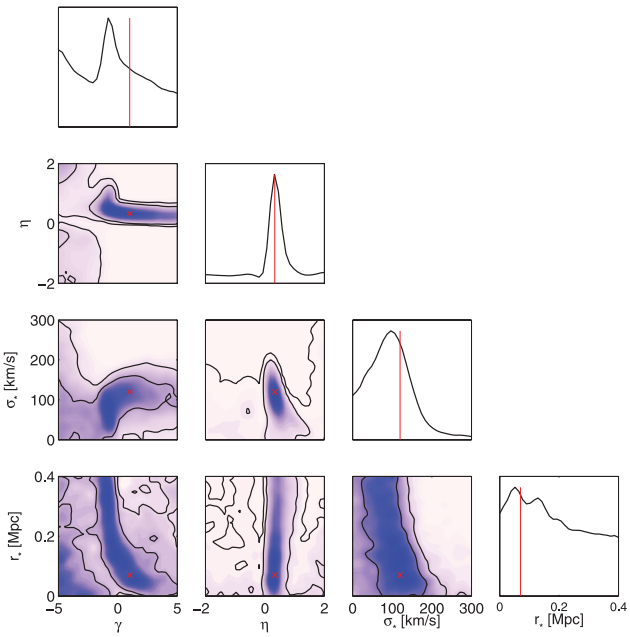

Figure 6. 1D and 2D marginalized posterior distributions for the parameters $\boldsymbol{h} = \{\gamma, \eta, \sigma_*, r_*\}$ of the truncated SIS halo model, derived from the analysis of 500 simulated SNIa data generated from a truncated SIS model (right). True parameter values are indicated by vertical lines and crosses in 1D and 2D plots, respectively. The SNIa sample used corresponds to that with the median value $\Delta \ln \mathcal{Z} = 0.1$ from the histogram in Fig. 5.

lensing signal. For this random sample, although the SIS halo model and the no-lensing model are essentially equally good descriptions of the data, according to the Bayesian evidence, one sees that most of the 1D and 2D marginalized posteriors have a well-defined peak (away from zero) that contains the true parameter values, indicating that reasonable constraints can be placed on the SIS halo parameters. Nonetheless, some of the 2D marginals exhibit pronounced degeneracies between the parameters, particular those involving the parameter r_*, which is the least well-constrained parameter. These features are consistent with the borderline value of $\Delta \ln \mathcal{Z}$ obtained for this sample.

In Fig. 7, we plot $\Delta \ln \mathcal{Z}$ as a function of the (symmetric positive and negative) limits on the uniform priors assumed for η and γ. In this case, the resulting variation is broadly what might be expected. It exhibits a well-defined two-dimensional peak corresponding roughly to the priors $\pi(\eta) = \mathcal{U}(-0.6, 0.6)$ and $\pi(\gamma) = \mathcal{U}(-1.2, 1.2)$, which are just wide enough to encompass the posterior probability mass associated with the peak centred on the true input values $\eta = 1/3$ and $\gamma = 1$. Indeed, for such priors, the log-evidence difference is $\Delta \ln \mathcal{Z} \approx 1.6$, indicating a 'substantial' preference for the SIS halo model. The evidence is lower for both narrower and wider priors on each parameter, since such priors, respectively, either exclude this probability mass or increase the prior volume without benefit.

6 APPLICATION TO REAL SUPERNOVAE DATA

We now apply our Bayesian analysis methodology to the real SNIa and galaxies data sets described in Section 4. We also investigate dividing the foreground galaxies in the SNLS catalogue into passive

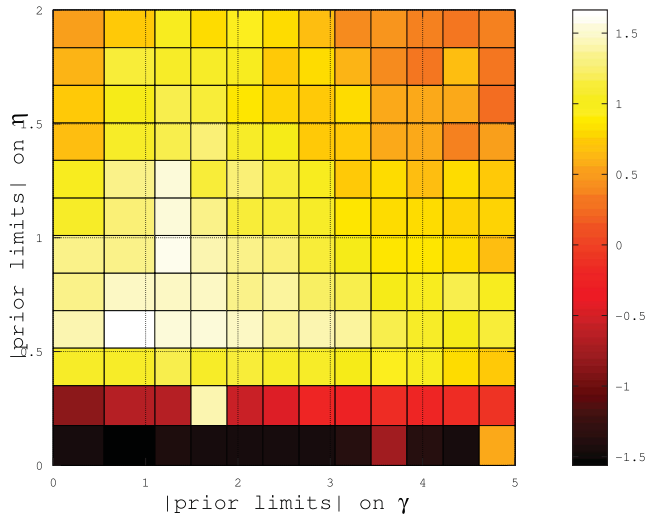

Figure 7. Log-evidence difference $\Delta \ln \mathcal{Z}$ between the SIS halo model and the null for the 'median' sample of 500 SNIa, as a function of the (symmetric positive and negative) limits on the uniform priors assumed for the parameters η and γ.

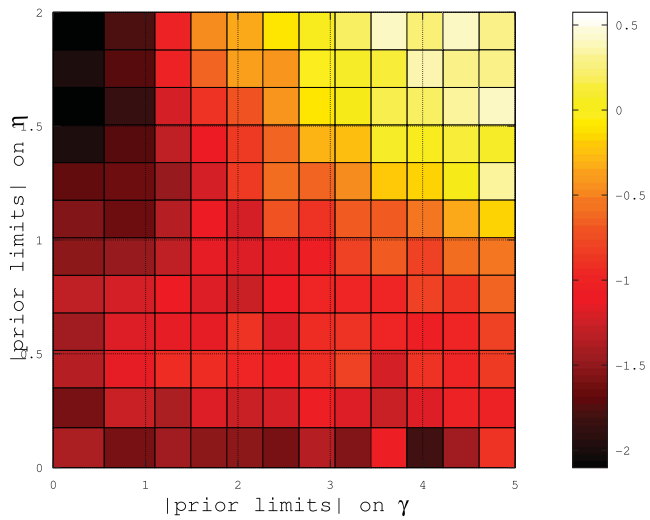

Figure 8. Log-evidence difference $\Delta \ln \mathcal{Z}$ between the SIS halo model and the null for the real SNLS3 sample of 162 SNIa, as a function of the (symmetric positive and negative) limits on the uniform priors assumed for the parameters η and γ.

and star-forming classes, each having SIS halo model parameters that are allowed to be independent.

Assuming a single galaxy type ($\boldsymbol{h}^{\rm p} = \boldsymbol{h}^{\rm sf}$), the log-evidence for the SIS halo model, relative to the null (no-lensing) model, is $\Delta \ln \mathcal{Z} = 0.2 \pm 0.2$, indicating a very marginal preference for the former. This is, however, only at the level of the uncertainty in the evidence calculation, and so this model and the no-lensing model are broadly equally favoured. When one splits the foreground galaxies into their passive and star-forming spectral types ($\boldsymbol{h}^{\rm p} \neq \boldsymbol{h}^{\rm sf}$), one obtains the slightly larger value $\Delta \ln \mathcal{Z} = 0.5 \pm 0.2$, but this still corresponds only to a marginal preference for the SIS halo model.

In Fig. 8 we plot $\Delta \ln \mathcal{Z}$ as a function of the (symmetric positive and negative) limits on the uniform prior assumed for η and γ, for the case in which $\boldsymbol{h}^{\rm p} = \boldsymbol{h}^{\rm sf}$. We see that, for this real data set, the resulting plot differs somewhat from that for the 'median' simulated

Downloaded from http://mnras.oxfordjournals.org/ at Stanford University on June 23, 2015

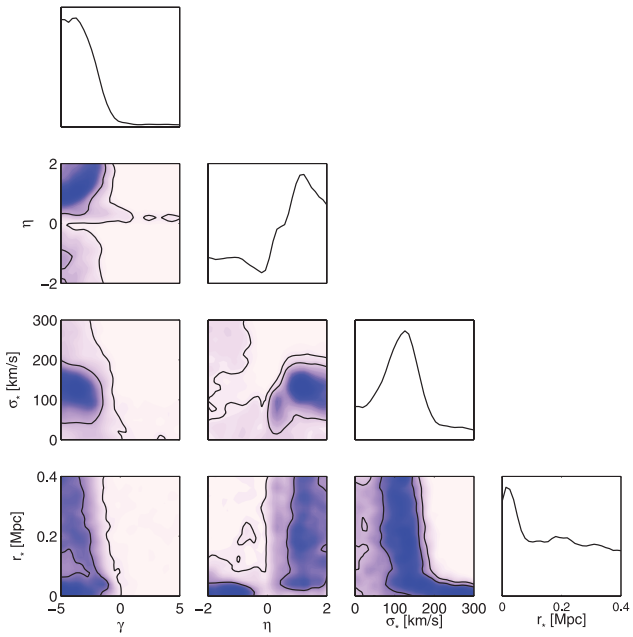

Figure 9. 1D and 2D marginalized posterior distributions for the parameters $\boldsymbol{h} = \{\gamma, \eta, \sigma_*, r_*\}$ of the truncated SIS halo model, derived from the analysis of real SNLS3 data.

sample containing 162 SNIa, given in Fig. 4, but does have some features in common. In particular, for priors on η narrower than about $\pi(\eta) = \mathcal{U}(-1, 1)$, there is almost no dependence on the width of $\pi(\eta)$ and only a very weak increase in $\Delta \ln \mathcal{Z}$ as $\pi(\gamma)$ widens. By contrast, if the prior on η is wider than about $\pi(\eta) = \mathcal{U}(-1, 1)$, there is a very strong dependence of $\Delta \ln \mathcal{Z}$ on the width of both $\pi(\eta)$ and $\pi(\gamma)$. The value of $\Delta \ln \mathcal{Z}$ falls rapidly with increasing width of $\pi(\eta)$, whereas is grows rapidly as $\pi(\gamma)$ widens. Indeed, it is only in the top right-hand corner of the plot that $\Delta \ln \mathcal{Z} > 0$, indicating that the SIS halo model is favoured over the no lensing model, albeit only marginally.

We discuss the halo parameters constraints for the two models ($\boldsymbol{h}^{\rm p} = \boldsymbol{h}^{\rm sf}$ and $\boldsymbol{h}^{\rm p} \neq \boldsymbol{h}^{\rm sf}$), in the following subsections.

6.1 Parameter constraints for a single galaxy type

The 1D and 2D marginalized parameter constraints obtained for the truncated SIS halo model with one galaxy type are shown in Fig. 9. We see that both the 1D and 2D constraints are somewhat tighter than those plotted in Fig. 3 for the 'median' simulated sample of 162 SNIa, which were very similar for simulations with and without a lensing signal. This may be indicative of a more pronounced, albeit weak, lensing signal in the real data, although the posterior distributions are still very broad. As might be expected, the parameter constraints are significantly less well-defined than those plotted in Fig. 6 for the 'median' simulated sample of 500 SNIa. It is worth noting, in particular, the form of the 2D marginal in the (γ,η)-subspace, for which this probability mass is concentrated in the top left-hand corner; this corresponds to large positive values of η and large negative values of γ, which is consistent with the dependence of $\Delta \ln \mathcal{Z}$ on the prior limits shown in Fig. 8.

Focusing on the 1D marginal posterior distribution of each halo parameter, we first note the strong preference for negative values of γ, as we observed in the analysis of simulations containing no lensing signal. As explained in Section 5, this is merely a consequence of the lensing signal (if any) in the data being very weak and does not constitute a meaningful constraint on the halo properties.

Conversely, there is a relatively strong preference for positive values of η, corresponding to a positive correlation between the halo velocity dispersion and luminosity. Indeed, the marginal distribution peaks at $\eta \approx 1$, which is considerably larger than the canonical values of $\eta^{\rm p} = \frac{1}{4}$ and $\eta^{\rm sf} = \frac{1}{3}$, corresponding to the Faber–Jackson and Tully–Fisher relations, valid for early and late-type galaxies, respectively. This constraint also differs noticeably from that shown in the left-hand panel of Fig. 3, obtained from simulated data containing no lensing signal, which is suggestive of a marginal lensing signal being present in the real data.

The possibility of a faint lensing signal being present in the data is also suggested by the 1D marginal distribution for the fiducial velocity dispersion σ_*, which has a clear peak away from zero. Indeed, the peak is centred on $\sigma_* \approx 120$ km s^{-1}, which was also the value assumed in the simulations analysed in Section 5. The fact that the parameter constraint obtained from the real data again appears tighter than that obtained from the simulations of 162 SNIa with no lensing signal, shown in the left-hand panel of Fig. 3, may be a result of the real data preferring $\eta \approx 1$, as opposed the value $\eta = \frac{1}{3}$ used in our simulations. From (13) and (14), one sees that the lensing signal produced by a halo with a given σ_* is larger in the former case.

Finally, we note that the 1D marginal for the fiducial truncation radius peaks very close to zero and yields no real constraint on r_*, as we found in our analysis of the 162 simulated SNIa.

6.2 Separating passive and star-forming galaxies

So far, we have assumed that the halo parameters for the truncated SIS and NFW models, respectively, are the same for different galaxy types. This may be an oversimplification and so it is of interest to split the foreground galaxies into their passive and star-forming spectral types, both of which are allowed to have independent halo parameters.

The galaxies in our sample are classified as either passive or star-forming depending on their specific star formation rate (sSFR) (see Section 4.2). We thus allow all the halo parameters to be different for each type of galaxy, so that the full halo parameter space becomes $\boldsymbol{h} = \{\gamma^{\rm p}, \eta^{\rm p}, \sigma_*^{\rm p}, r_*^{\rm p}, \gamma^{\rm sf}, \eta^{\rm sf}, \sigma_*^{\rm sf}, r_*^{\rm sf}\}$. The fraction of passive galaxies ranges from 5 per cent in the CFHTLS fields D1 and D3 to 8 per cent in field D4. Thus, the vast majority of foreground galaxies are star forming.

The resulting 1D and 2D marginalized posteriors for the parameters are shown in Fig. 10. One sees that the constraints on the parameters for passive and star-forming galaxies are very different. As one might expect, given the relative percentages of passive and star-forming galaxies in the catalogue, the constraints on the halo parameters of the passive galaxies are very much weaker than those for star-forming galaxies. Indeed, for the passive galaxies, the marginal distributions closely resemble those shown in Fig. 3, obtained from simulations containing 162 SNIa with no lensing signal. Conversely, for star-forming galaxies, the constraints are slightly tighter than those shown in Fig. 9, obtained from the real data assuming just one galaxy type, but resemble them in their main features. In particular, we again see a strong preference for negative values of $\gamma^{\rm sf}$, but now the 1D marginal distribution has a modest peak at $\gamma^{\rm sf} \approx -3$. We also recover a strong constraint

Downloaded from http://mnras.oxfordjournals.org/ at Stanford University on June 23, 2015

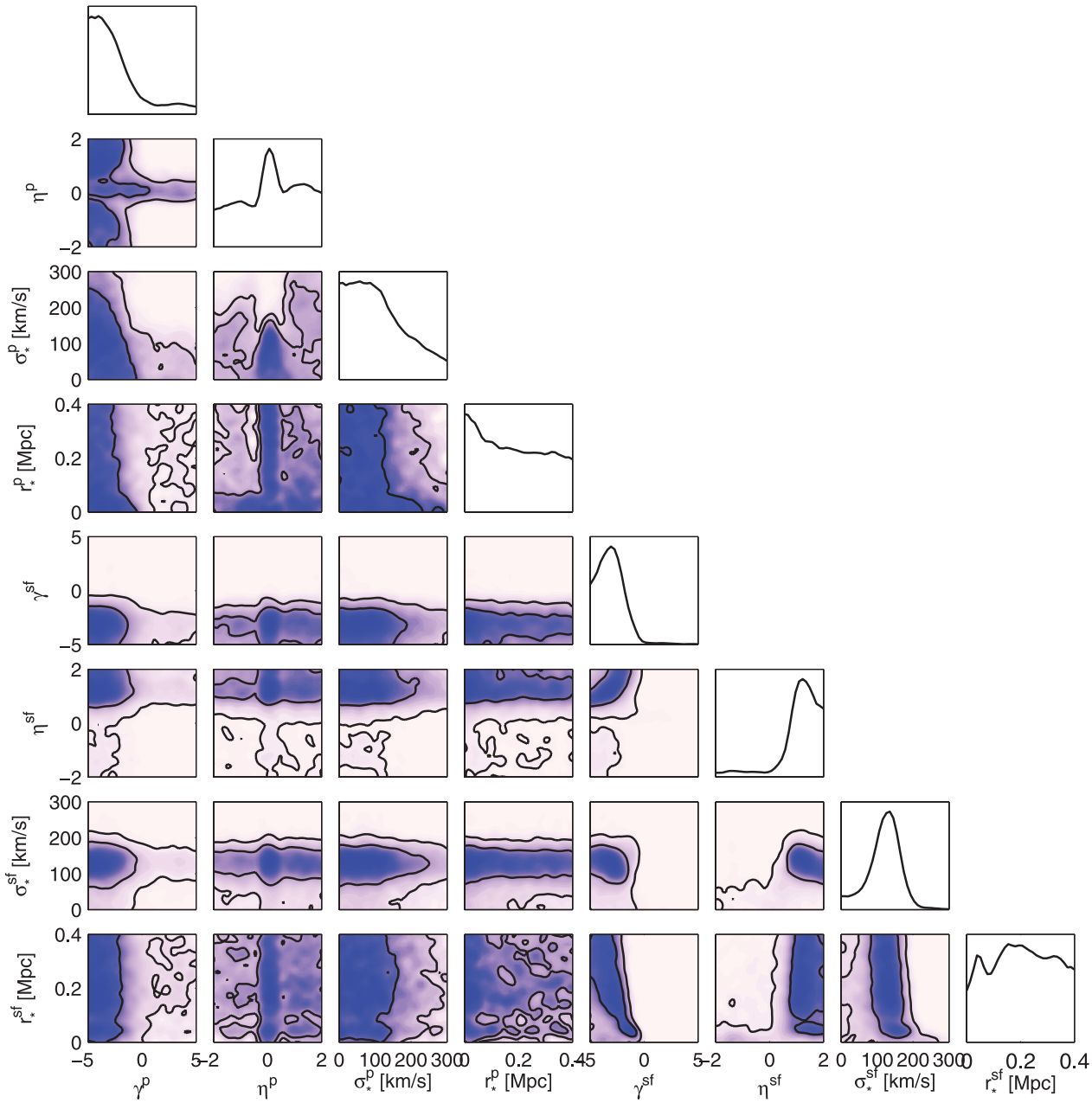

Figure 10. 1D and 2D marginalized posterior distributions for the parameters $\boldsymbol{h} = \{\gamma^{\rm p}, \eta^{\rm p}, \sigma_*^{\rm p}, r_*^{\rm p}, \gamma^{\rm sf}, \eta^{\rm sf}, \sigma_*^{\rm sf}, r_*^{\rm sf}\}$ of the truncated SIS halo model for passive and star-forming galaxies, respectively, derived from the analysis of real SNLS3 data.

that $\eta^{\rm sf}$ is positive, with the 1D marginal possessing a small peak at $\eta^{\rm sf} \approx 1$. The 1D marginal for $\sigma_*^{\rm sf}$ peaks strongly away from zero, preferring a value of $\sigma_*^{\rm sf} \approx 150$ km s^{-1}. There is, however, no constraint on $r_*^{\rm sf}$, which is in keeping with our previous findings.

Finally, it is worth noting that the 2D marginal in the $(\sigma_*^{\rm p}, \sigma_*^{\rm sf})$-space shown in Fig. 10 bears a passing resemblance to the corresponding plot (Fig. 6) in Jönsson et al. (2010b), but only if $\sigma_*^{\rm p}$ and $\sigma_*^{\rm sf}$ are interchanged. Given the relative percentages of passive and star-forming galaxies in the catalogue, it seems sensible that one should obtain a tighter constraint on $\sigma_*^{\rm sf}$ than $\sigma_*^{\rm p}$, as we find in Fig. 10. By contrast, fig. 6 in Jönsson et al. (2010b) shows the opposite, which suggests that they have erroneously swapped the galaxy types in their analysis.

6.3 Inclusion of additional low-redshift supernovae data

We also investigate the inclusion of additional, low-redshift SNIa data to our analysis as a potential means of enhancing the detection of a halo lensing signal. The rationale here is first to analyse the low-z SNIa data alone, using precisely the same methodology as for the SNLS3 data, but assuming no lensing from foreground galaxy haloes. The resulting posterior distributions derived for (most of) the nuisance parameters listed in Table 1 may then be used as priors on these parameters in the subsequent analysis of the (high-z) SNLS3 data, thereby replacing the very conservative priors assumed in Table 1, which may be 'diluting' the lensing signal.

As our low-z SNIa data set, we use an updated version of the catalogue compiled by Sullivan et al. (2010). This consists of a sample

Downloaded from http://mnras.oxfordjournals.org/ at Stanford University on June 23, 2015

from the compilation of Conley et al. (2011), which itself includes SNIa from a variety of sources, primarily Hamuy et al. (1996), Riess et al. (1999), Jha et al. (2006), Hicken et al. (2009), Contreras et al. (2010). Sullivan et al. (2010) apply bulk-flow peculiar velocity corrections to the SN magnitudes and redshifts, placing the redshifts in the CMB-frame ($z_{\rm cmb}$) following Neill, Hudson & Conley (2007), but with updated models ((Conley et al. 2011)). Only SN Ia in the smooth Hubble flow, defined as $z_{\rm cmb} > 0.01$, are used, and the same light-curve quality cuts as for the SNLS3 sample are employed. There are 123 low-redshift SN Ia in total, with redshifts in the range [0.01, 0.08].

An analysis of these data yields approximately Gaussian posteriors (truncated to positive values) on the nuisance parameters, given by: $\alpha \sim \mathcal{N}(1.30, 0.11^2)$, $\beta \sim \mathcal{N}(2.81, 0.18^2)$, $R_x \sim \mathcal{N}(0.119, 0.008^2)$ and $R_{\rm c} \sim \mathcal{N}(0.074, 0.05^2)$. These distributions are clearly much tighter than the original assumed priors given in Table 1; note that we use the original prior on the nuisance parameter $\sigma_{\rm int}$, as this quantity is likely to differ between low-z and high-z SNIa, since observational uncertainties such as the estimation of photometric errors can lead to variations of $\sigma_{\rm int}$ on a sample-by-sample basis (March et al. 2012). We find that using the posteriors derived from the low-z SNIa as priors in the subsequent analysis of the high-z SNLS3 data yields parameter constraints that are almost identical to those presented in Figs 9 and 10. Moreover, the log-evidences relative to the null (no-lensing) model are found to be very similar to those obtained previously. This finding makes sense, since the new, tighter priors on the nuisance parameters are used for both the halo and null (no-lensing) models, and they are, in fact, consistent with the posteriors derived on these parameters from the SNLS3 data alone. Thus, in summary, our results are unchanged by the inclusion of low-z SNIa data.

7 CONCLUSIONS

We have presented a Bayesian statistical methodology for constraining the properties of dark matter haloes of foreground galaxies that intersect the lines of sight towards SNIa. The method builds upon the Bayesian hierarchical model presented by March et al. (2011) for improving constraints on cosmological parameters from SNIa observations. Compared with the usual χ^2-method, which suffers from shortcomings in terms of its statistical foundations and robustness, March et al. (2011) demonstrate that the Bayesian method delivers tighter statistical constraints, reduces statistical bias and produces confidence intervals with better statistical coverage.

We use this methodology to obtain an effective likelihood function giving the probability of obtaining the observed SNIa data (i.e. the parameter values obtained in SALT-II light-curve fits) as a function of the parameters of the dark matter halo models assumed for the galaxies along the lines of sight to the SNIa. Following the imposition of suitable priors on these parameters (together with some nuisance parameters), we explore the full posterior distribution in all the parameters simultaneously using the nested sampling algorithm MultiNest, which also calculates the Bayesian evidence for use in model comparison.

We first apply our method to simulated SNIa data sets generated using 162 high-redshift ($0.1 \lesssim z \lesssim 1$) SNIa from the SNLS3 as a template and assuming a truncated SIS model for the dark matter halo density profile of foreground galaxies in the deep CFHTLS fields. These simulations were generated using the SNANA package, assuming realistic values for the halo parameters and observational data quality. Assuming conservative priors on the parameters, we demonstrate that there is a wide variation in the significance at which one may detect a gravitational lensing signal, depending on whether the sample contains some SNIa that are strongly magnified. Indeed, the log-evidence $\Delta \ln \mathcal{Z}$, relative a model assuming no lensing, ranges from about -1.5 to 4.5, with a median value of -0.6. For this median catalogue, the parameter constraints are very broad and resemble those obtained from analysing a simulation containing no lensing signal.

Analysing simulated catalogues containing 500 SNIa, we again find a wide variation in the significance to which one may detect the lensing signal, depending on the number of highly magnified SNIa contained in the sample. Nonetheless, as might be expected in this case, the distribution of $\Delta \ln \mathcal{Z}$ is shifted to larger values, ranging from about -2 to 13, with a median value of 0.1. For this median sample, our method produces posterior distributions for the parameters that have well-defined peaks, which contain the true input values used in the simulations. This demonstrates that our method can indeed detect the lensing signal and estimate the halo parameter values correctly, provided one analyses a sufficient number of SNIa.

In the analysis of real SNLS3 data (consisting of 162 SNIa) we find, contrary to previous studies, only a very marginal detection of a lensing signal in the case of the truncated SIS halo model. Assuming conservative priors on the halo parameters, the model is preferred by just 0.2 log-evidence units relative to the no lensing model. Indeed, since this difference is similar to the uncertainty in the evaluation of the evidence, one may consider the no lensing model to be equally favoured by the data. We also show that assuming narrower priors centred on zero for the exponents η and γ of the assumed power-law relations between velocity dispersion, luminosity and truncation radius leads to *smaller* log-evidence values. Nonetheless, the parameter constraints for the truncated SIS halo model do appear somewhat tighter than those obtained for simulations of 162 SNIa without the inclusion of a lensing signal, which is again suggestive of a borderline detection of a lensing signal in the real SNLS3 data. One finds that the SNLS3 data strongly prefer negative values of γ, which corresponds to luminous galaxies having smaller truncation radii than less luminous ones, but this is simply a manifestation of the lensing signal being very weak and does not constitute a meaningful constraint on the halo properties. There is also a preference for positive values of η, corresponding to a positive correlation between the halo velocity dispersion and luminosity, with the 1D marginal for this parameter peaking at $\eta \approx 1$, which is somewhat larger than the canonical values of $\eta^{\rm p} = \frac{1}{4}$ and $\eta^{\rm sf} = \frac{1}{3}$ valid for early- and late-type galaxies, respectively, and leads to a stronger lensing signal for a halo with a given luminosity. The 1D marginal distribution for the fiducial velocity dispersion σ_* has a clear peak away from zero, which is centred on $\sigma_* \approx 120$ km s^{-1}, but the marginal for the fiducial truncation radius peaks very close to zero and yields no real constraint on r_*.

Finally, we investigate the possibility that the halo parameters may be different for passive and star-formation galaxies, respectively. Focusing on the truncated SIS model, we find that allowing all the halo parameters for the two galaxy types to be completely independent increases the evidence for the model slightly, by 0.3 log-evidence units. Since only around 5 per cent of the galaxies in our catalogue are passive, we find that one cannot place any meaningful constraints on their halo properties, but that the constraints on the halo parameters of the star-forming galaxies are similar to those obtained if one assumes just one galaxy type.

Our results contradict to some extent the previously reported high-significance detections of gravitational lensing of SNIa (Jönsson et al. 2007; Kronborg et al. 2010; Jönsson et al. 2010a,b),

Downloaded from http://mnras.oxfordjournals.org/ at Stanford University on June 23, 2015

where the last study uses essentially the same SNLS3 data as those analysed here. We have also verified that our findings are unchanged by the inclusion of additional low-z SNIa data. The major difference between these earlier analyses and the study presented here is the statistical methodology employed. As demonstrated by March et al. (2011), the usual χ^2-method used in previous analyses has a number of shortcomings in terms of its statistical foundations and robustness, including not allowing for rigorous model checking and not providing a reliable framework for the evaluation of systematic uncertainties. This should be contrasted with the statistically principled and rigorous Bayesian hierarchical model used here. Moreover, previous studies employed simple gridding methods to explore the parameter space of the dark matter halo models, which allow only a small subset of the parameters to be varied simultaneously. In particular, Kronborg et al. (2010) fix all the halo parameters to 'reasonable' values to derive a statistical significance for the presence of a lensing signal.

It should be mentioned that the analysis presented here does make the significant simplifying assumption that all dark matter haloes of the foreground galaxies have the same values for their free parameters (at least within their spectral type). This is not too restrictive an assumption, however, for free parameters corresponding to fiducial values appearing in scaling laws, but it is certainly an oversimplification. This may weaken the constraints in the analysis of real data, as compared with the analysis of simulated data generated assuming all the haloes to have the same parameter values. We will investigate this possibility in a future work.

Concluding the paper, we note that the analysis code used in this paper is quite general in nature and could easily be applied to other combinations of SNIa and foreground galaxy catalogues. Anyone wishing to use the code in collaboration should contact the authors.

ACKNOWLEDGEMENTS

NVK thanks Jakob Jönsson for his invaluable help in the initial stages of this work, Mark Sullivan for providing the foreground galaxy catalogues and for many useful discussions, Ariel Goobar for reading through an early draft of the paper and providing insightful comments, and Joakim Edsjö for his support and encouragement throughout. NVK also acknowledges support from the Swedish Research Council (contract No. 621-2010-3301). MCM thanks Rick Kessler and John Marriner for assistance with simulating and analysing SNANA data. FF is supported by a Research Fellowship from Trinity Hall, Cambridge. This work was performed on COSMOS VIII, an SGI Altix UV1000 supercomputer, funded by SGI/Intel, HEFCE and PPARC.

REFERENCES

Astier P. et al., 2006, A&A, 447, 31
Balland C. et al., 2009, A&A, 507, 85
Bergström L., Goliath M., Goobar A., Mörtsell E., 2000, A&A, 358, 13
Boulade O. et al., 2003, in Iye M., Moorwood A. F. M., eds, SPIE Conf. Ser. Vol. 4841, MegaCam: the New Canada–France–Hawaii Telescope Wide-field Imaging Camera. p. 72
Bridges M., Feroz F., Hobson M. P., Lasenby A. N., 2009, MNRAS, 400, 1075
Bronder T. J. et al., 2008, A&A, 477, 717
Conley A. et al., 2006, ApJ, 644, 1
Conley A. et al., 2011, ApJS, 192, 1
Contreras C. et al., 2010, AJ, 139, 519
Dodelson S., Vallinotto A., 2006, Phys. Rev. D, 74, 063515
Faber S. M., Jackson R. E., 1976, ApJ, 204, 668
Feroz F., Hobson M. P., 2008, MNRAS, 384, 449
Feroz F., Hobson M. P., 2012, MNRAS, 420, 596
Feroz F., Hobson M. P., Bridges M., 2009, MNRAS, 398, 1601
Feroz F., Gair J. R., Graff P., Hobson M. P., Lasenby A., 2010, Classical Quantum Gravity, 27, 075010
Feroz F., Balan S. T., Hobson M. P., 2011, MNRAS, 415, 3462
Frieman J. A., 1996, Comments Astrophys., 18, 323
Guy J., Astier P., Baumont S., Hardin D., Pain R., Regnault Ruhlmann-Kleider V., 2007, A&A, 466, 11
Guy J. et al., 2010, A&A, 523, A7
Hamuy M., Phillips M. M., Suntzeff N. B., Schommer R. A., Maza J., Aviles R., 1996, AJ, 112, 2391
Hicken M., Wood-Vasey W. M., Blondin S., Challis P., Jha S., Kelly P. L., Rest A., Kirshner R. P., 2009, ApJ, 700, 1097
Hobson M. P., McLachlan C., 2003, MNRAS, 338, 765
Holz D. E., Wald R. M., 1998, Phys. Rev. D, 58, 063501
Howell D. A. et al., 2005, ApJ, 634, 1190
Jha S. et al., 2006, AJ, 131, 527
Jha S., Riess A. G., Kirshner R. P., 2007, ApJ, 659, 122
Jönsson J., Dahlén T., Goobar A., Mörtsell E., Riess A., 2007, J. Cosmol. Astropart. Phys., 6, 2
Jönsson J. et al., 2008, A&A, 487, 467
Jönsson J., Dahlén T., Hook I., Goobar A., Mörtsell E., 2010a, MNRAS, 402, 526
Jönsson J. et al., 2010b, MNRAS, 405, 535
Kantowski R., Vaughan T., Branch D., 1995, ApJ, 447, 35
Kessler R. et al., 2009, preprint (arXiv:0908.4280)
Kowalski M. et al., 2008
Kronborg T. et al., 2010, A&A, 514, A44
Liddle A. R., 2007, MNRAS, 377, L74
Mandel K. S., Wood-Vasey W. M., Friedman A. S., Kirshner R. P., 2009, ApJ, 704, 629
Mandel K., Kirshner R. P., Narayan G., Wood-Vasey W. M., Friedman A. S., Hicken M., 2010, BAAS, 42, 343.05
March M. C., Trotta R., Berkes P., Starkman G. D., Vaudrevange P. M., 2011, MNRAS, 418, 2308
March M. C., Karpenka N. V., Feroz F., Hobson M. P., 2012, MNRAS, submitted
Metcalf R. B., 1999, MNRAS, 305, 746
Metcalf R. B., Silk J., 1999, ApJ, 519, L1
Navarro J. F., Frenk C. S., White S. D. M., 1997, ApJ, 490, 493
Neill J. D., Hudson M. J., Conley A., 2007, ApJ, 661, L123
Perrett K. et al., 2010, AJ, 140, 518
Phillips M. M., 1993, ApJ, 413, L105
Rauch K. P., 1991, ApJ, 374, 83
Riess A. G. et al., 1999, AJ, 117, 707
Riess A. G. et al., 2004, ApJ, 607, 665
Riess A. G. et al., 2007, ApJ, 659, 98
Sarkar D., Amblard A., Holz D. E., Cooray A., 2008, ApJ, 678, 1
Schneider P., Ehlers J., Falco E. E., 1992, Gravitational Lenses. Springer-Verlag, New York
Skilling J., 2004, in Fischer R., Preuss R., Toussaint U. V., eds, AIP Conf. Ser. Nested Sampling. Am. Inst. Phys., New York, p. 395
Strolger L.-G. et al., 2004, ApJ, 613, 200
Sullivan M. et al., 2006, ApJ, 648, 868
Sullivan M. et al., 2010, MNRAS, 406, 782
Trotta R., 2007, MNRAS, 378, 72
Tully R. B., Fisher J. R., 1977, A&A, 54, 661
Wambsganss J., Cen R., Xu G., Ostriker J. P., 1997, ApJ, 475, L81
Wang L., Goldhaber G., Aldering G., Perlmutter S., 2003, ApJ, 590, 944
Zentner A. R., Bhattacharya S., 2009, ApJ, 693, 1543

This paper has been typeset from a TEX/LATEX file prepared by the author.

Downloaded from http://mnras.oxfordjournals.org/ at Stanford University on June 23, 2015